

Indentation crack initiation in ion-exchanged aluminosilicate glass

D. J. MORRIS, S. B. MYERS,* R. F. COOK

Department of Chemical Engineering and Materials Science, University of Minnesota, Minneapolis, MN 55455, USA

E-mail: dmorris@cems.umn.edu

The threshold load for crack initiation resulting from Vickers indentation is investigated in chemically tempered aluminosilicate glass. Aluminosilicate glass was ion-exchanged in a potassium nitrate salt bath at temperatures of 380, 400, and 420°C for times ranging from two to sixty minutes. The ion-exchange profiles were investigated using an electron microprobe, and the diffusion coefficients and activation energy for ion-exchange elucidated. Residual stresses were not measured directly, but were estimated using an indentation fracture analysis. A physically-based fracture model is developed to describe the threshold indentation load data. From kinetic and indentation threshold models, predictions of crack initiation thresholds are made over a wide range of ion-exchange conditions. © 2004 Kluwer Academic Publishers

1. Introduction

Chemical tempering (ion-exchange) is one of many methods for strengthening glasses [1, 2]. Na⁺-K⁺ exchange in aluminosilicate glasses introduces compressive stresses at the surface, and these stresses act as an effective toughening mechanism [3, 4], thereby increasing the strength. However, the susceptibility of a brittle material to damage initiation from handling and service conditions (such as abrasion or particle impact) is, in many ways, as important a design metric as the toughness of the material (resistance to flaw propagation). Indentation is a useful technique for studying the mechanics of damage initiation under abrasive or particle impact conditions [5, 6]. This work explores the effect of ion-exchange time and temperature over a broad range of conditions on the load threshold for radial crack initiation (the indentation load beneath which radial cracks will not form) from Vickers indentation.

Fig. 1 is an example of this phenomenon. Fig. 1a is an untreated aluminosilicate glass indented with a Vickers indenter at a load of 150 N. Radial cracks have formed at the corners of the indentation impression. Such cracks lie perpendicular to the material surface, and are considered to be representative of strength-controlling flaws. Fig. 1b is the same glass, subjected to ion-exchange and indented under the same conditions. The compressive surface stresses have suppressed cracking at the site [7–10]. This is a clear demonstration that compressive surface stresses not only have the capability to strengthen a glass with an existing flaw population, but also reduce susceptibility to further strength degradation due to service. Cracks responsible for chipping and wear (lateral cracks) are not considered in this work.

A fracture-mechanics based model is developed that links the depth and magnitude of the ion-exchange stresses to the indentation cracking threshold. There are many existing models that describe the mechanics of the load threshold [7, 11–13]. The load threshold model in this work is based on an indentation crack-threshold and crack-extension model developed by Cook and Braun [13], developed for the homogeneous toughening of phase transformation. The model here is extended to the inhomogeneous toughening mechanism of surface stresses. In fact, the scales of the ion-exchange stress profile and shear-nucleated indentation flaw nuclei are similar, and therefore the details of the inhomogeneous distribution of residual stresses become crucial to a description of the phenomenon. From diffusional kinetic data measured from the array of exchange conditions, and the indentation threshold model, predictions about the general effect of time and temperature of exchange on the indentation cracking threshold are made.

2. Experimental procedure

2.1. Ion-exchange and diffusion profile measurement

Aluminosilicate (ALS) glass (Code 0317, Corning Glass Works, Corning, NY), 2.2 mm thick, was chosen because of the ease of Na⁺-K⁺ ion-exchange in aluminosilicate glasses [1, 2, 14], and for comparison to other ion-exchange mechanical strengthening work [9].

A series of three exchange temperatures, chosen to be above the melting point of the bath salt (KNO₃) but well below the softening point of ALS were used, with

* Present address: Department of Chemical Engineering, Princeton University, Princeton, NJ 08544, USA.

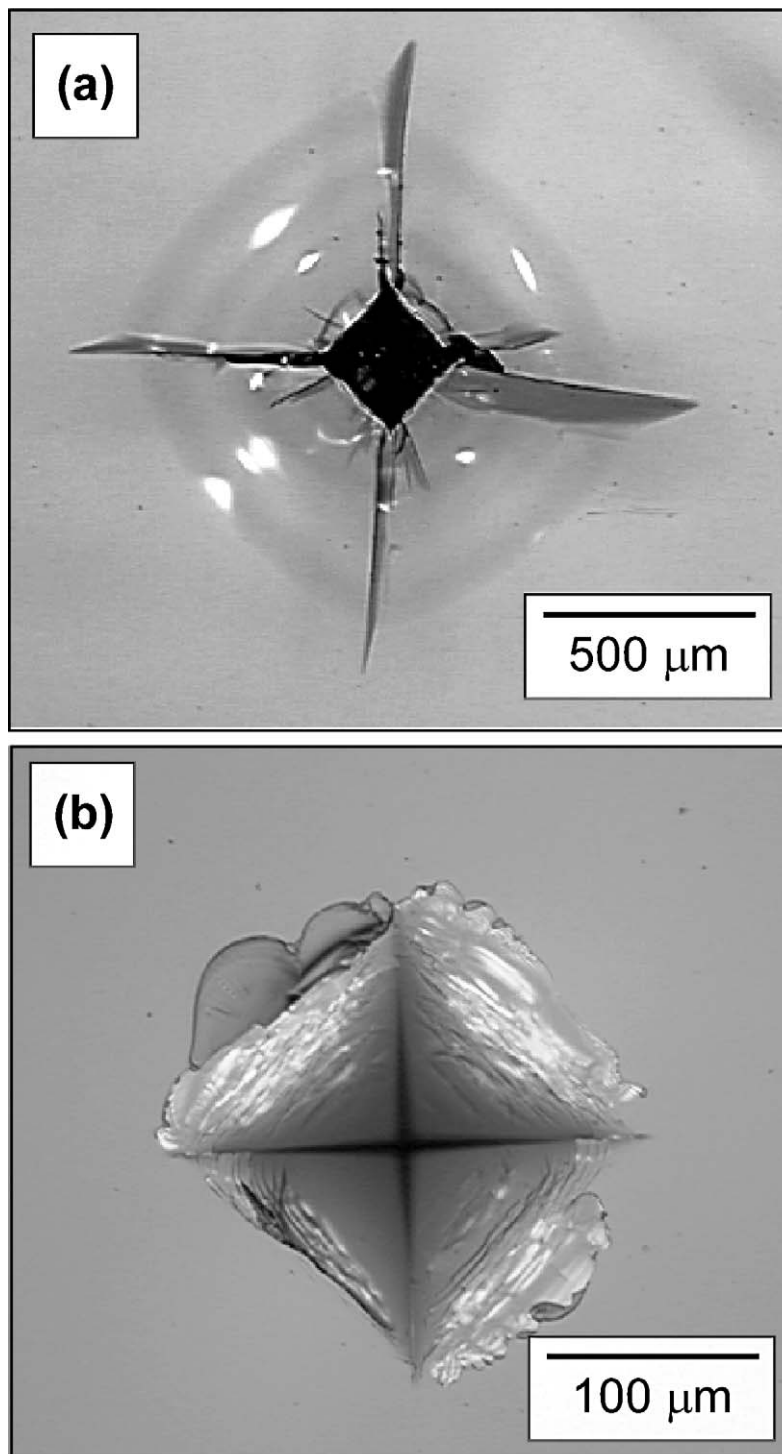


Figure 1 (a) An optical micrograph of a 150 N indentation on unexchanged ALS glass with radial cracks emanating from the impression corners. (b) A micrograph of a 150 N indentation on ALS ion-exchanged at 400°C for 30 min. Radial cracking is suppressed by the compressive surface stresses generated by the ion-exchange process. The surface traces of shear faults are visible in this micrograph.

six different exchange times at each temperature. The treatment conditions are listed in Table I. Ion-exchange was performed in a commercial salt bath (Mini-60, Kirk Optical Co. Freeport, NY), modified to use a digital

TABLE I Ion-exchange conditions

Temperature (°C)	Exchange times (min)
380	2, 5, 10, 20, 30, 60
400	2, 5, 11.5, 20, 30, 61
420	2, 5, 10, 20, 30, 60

temperature controller with a thermocouple. The temperature of the bath was stabilized for at least one hour in all experiments before the exchange process began. The glass was held approximately 10 cm above the molten salt for ten minutes before and after immersion in the bath to avoid thermal shock damage. After exchange, the glass was rinsed under tap water to remove residual frozen salt from the surface.

Ion concentration profiles near the surface were measured with an electron microprobe (JEOL 8900 Electron Probe Microanalyzer). Beam conditions for all experiments were 10 nA current and 10 kV accelerating

TABLE II Nominal and observed ALS compositions

Molecular concentration (%)	SiO ₂	Al ₂ O ₃	K ₂ O	Na ₂ O	CaO	MgO	TiO ₂
Nominal	67.42	10.46	2.40	13.43	0.31	5.26	0.61
Experimental	67.9	10.5	2.5	12.9	0.4	5.1	0.7

voltage. Calibration of the X-ray spectrum to molecular concentrations was performed with glassy geological standards. All known ionic components (except Fe₂O₃ and SnO₂, which are the most dilute species at 0.10 and 0.02% molecular concentrations, respectively) were measured simultaneously to verify that Na⁺ and K⁺ were the only mobile species. Table II demonstrates the excellent agreement between the observed and nominal molecular compositions of ALS.

A difficulty in making ion-concentration measurements is that sodium is easily liberated from the glassy matrix by a bright, high-energy electron beam. When working with the very small beam spots (<1 μm) required to measure ion diffusion profiles in the glass, the characteristic sodium signal was observed to decay significantly over the course of several seconds, making precise composition measurements difficult. To avoid sodium “burn-out” affecting composition measurements, the following scheme, shown schematically in Fig. 2, was used to perform ion composition profile measurements. The surface ion concentrations, C_s , were measured quantitatively with a broad 30 μm beam with a dwell time of 60 s. At these conditions, the beam is weak enough such that decay of the Na⁺ signal is not observed. The Bethe range of electron penetration was calculated as approximately 1.3 μm at these beam conditions [15, 16], and therefore the measured surface concentrations are approximately representative of this depth.

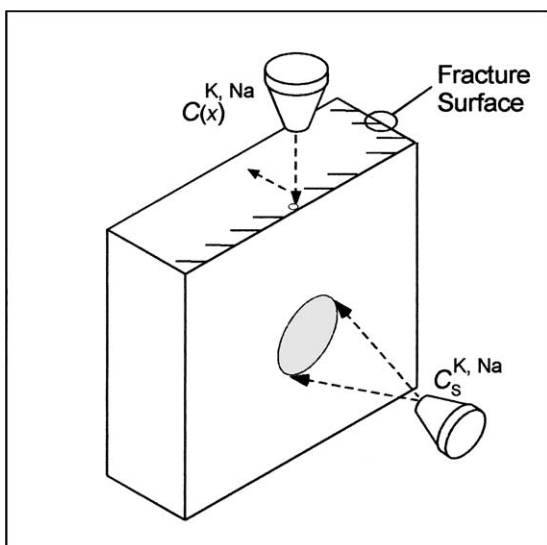


Figure 2 The experimental procedure for determining the surface concentrations and diffusion profiles for components of ALS glass. The surface concentration, C_s , is determined by using a broad beam for a long time. Composition profiles, $C(x)$, as a function of depth, x , into the bulk are obtained by scanning a fracture surface at high speed to avoid sodium “burn-out”.

Concentration profiles were then measured by scanning a cross-section of glass, formed via cleavage, from the surface up to 100 μm into the interior of the glass. Again, this is shown schematically in Fig. 2. Scans were performed three times at different locations on the cleaved surface. The beam spot size was approximately 1 μm and the dwell time was 1 s. The dwell time was too short for accurate quantitative measurement of ionic concentrations. Instead, the surface and bulk *relative* “concentrations” (X-ray counts) from the cross-sectional scans were matched to the measured concentrations at the surface and the bulk, and the relative concentration profiles were used to generate the ion concentration profile in the glass. Within the resolution of the microprobe experiment, the concentration profiles indicate that only Na⁺ and K⁺ were mobile to any significant degree during the diffusion process.

2.2. Indentation cracking threshold measurements

For each of the ion-exchange time-temperature combinations in Table I, the threshold indentation load for cracking with a Vickers indenter (in ambient air) was found. A gravity-loaded indenter (Zwick Model 3212) with a full-scale capacity of 300 N was used for all experiments. For each sample, indentations were first performed over a coarse range of loads. Subsequent indentations were performed using a narrowed range until the threshold load was determined to within a 15 N resolution.

Crack formation at a sharp indentation site is a stochastic process [10, 17], and there is slight variability in the cracking behavior of indentations formed under ostensibly identical conditions. Therefore, a definition of the “threshold” load for cracking, P_{th} , must take this variability into account. For the purposes of this work, the threshold load for cracking was defined as the load at or above which 60% of the possible radial cracks (five indentations per indentation load, with one radial crack formation site at the each of the four corners of the impression) formed (within the resolution of the indentation experiments). Fig. 3 is a representative plot of the percentage of radial cracks formed as a function of indentation load for a total of five indentations per load, with the above definition of the threshold load shown graphically. While the definition applies strictly to the percentage of radial cracks formed at potential sites, it was observed that cracks usually formed at all corners of the impression, or at none. So, roughly, P_{th} is the load at which three out of five indentations exhibited radial cracking.

2.3. Surface stress estimation

The surface stress distribution in the glasses resulting from ion-exchange, $\sigma(x)$, was not measured directly. An indentation crack length technique [18, 19] was used to estimate the stresses at the surface. Crack lengths were measured only near the threshold indentation load; there was not a characterization of crack-length as a function of indentation load for each system.

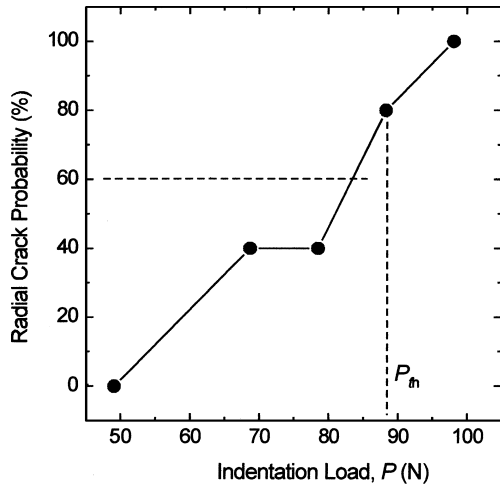


Figure 3 Plot of the probability of radial crack initiation vs. indentation load for an ALS glass ion-exchanged at 380°C for 5 min. The threshold load for cracking, P_{th} , is defined as the load at or above which radial cracks form at 60% of prospective indentation sites. Each point represents the average of five indentation experiments, or 20 radial crack formation sites.

This technique has been used with some success, although previous results from ion-exchanged glass [19] and ion-implanted ceramics and glasses [20, 21] show that there can be a significant underestimation of the surface stresses. This is discussed further in the Results section.

3. Results

3.1. Ion diffusion measurement

While there are two mobile species counter-diffusing in the ion-exchange process studied here, charge neutrality requires that the diffusion rate be limited by the slowest species, believed to be the heavier, larger K^+ ion [22]. Therefore, when the glass is much thicker than any characteristic diffusion length, ion diffusion may be treated as a one-dimensional single-species diffusion process. One-dimensional diffusion in a Cartesian space is described by

$$C(x) = (C_s - C_\infty) \left[1 - \operatorname{erf} \left(\frac{x}{2\sqrt{Dt}} \right) \right] + C_\infty, \quad (1)$$

where x is the spatial coordinate with origin at the surface of the glass, C_s is the surface concentration, C_∞ is the original concentration (the concentration within the bulk of the glass), D is the diffusion coefficient and t is time. Fig. 4 is a representative plot of concentration data with fits of Equation 1. Because the surface and bulk concentrations were measured and used to generate the concentration profiles from qualitative scan data, only D was allowed to vary in making such fits to the diffusion profiles. While fits to both K^+ and Na^+ data generate similar values for the diffusion coefficient, estimates of D from the K^+ data are used exclusively hereupon because of the lower noise and greater expected accuracy of the measurement of K^+ , evident from Fig. 4. Monte Carlo simulations [16] show that the probed diameter of the X-ray signal for the $K K_\alpha$ peak (~ 3.3 keV) in a silica matrix should spread ap-

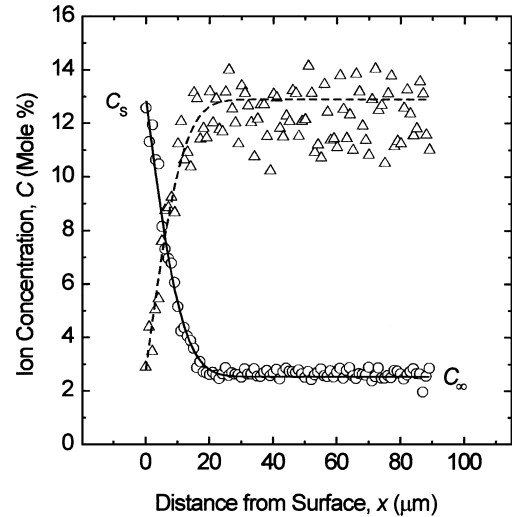


Figure 4 Representative plot of Na^+K^+ ion-exchange concentration profiles in ALS glass, from a 400°C—60 min exchange. Plotted with the experimental data is a fit of Equation 1 to both Na^+ and K^+ data. The surface concentration C_s and bulk concentration C_∞ are indicated for K^+ .

proximately 1.1 μm . Although repeated profile scans were indistinguishable, uncertainty in the determination of the location of the surface and beam spread in the material make the practical spatial resolution on the order of 1.5 μm . Measured diffusion coefficients are in the range 10^{-14} – 10^{-15} $m^2 s^{-1}$, which agree with other measurements of Na^+K^+ diffusion coefficients in aluminosilicate glasses [23].

The diffusion coefficient as a function of temperature allows estimation of the activation energy for diffusion, Q , through

$$D = D_0 \exp \left(-\frac{Q}{kT} \right), \quad (2)$$

where k is Boltzmann's constant, T is temperature and D_0 is the diffusion coefficient prefactor. Fig. 5 is a plot

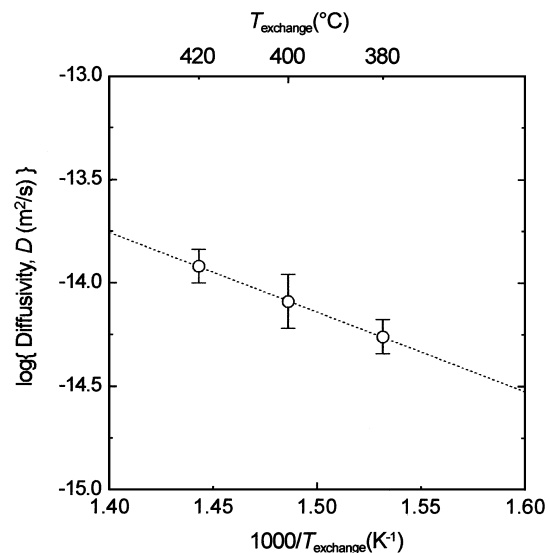


Figure 5 Logarithm of the measured diffusion coefficient, D , plotted as a function of the reciprocal of the temperature. Diffusion coefficients are averages from ion-exchanges in the 20–60 min range. A fit of the diffusion data, shown as a dashed line, to Equation 2 estimates the activation energy for diffusion as 0.75 eV.

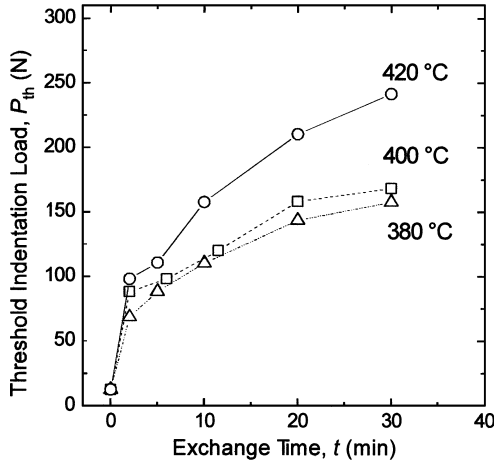


Figure 6 Threshold indentation load as a function of Na⁺-K⁺ ion-exchange time for ALS glass at the exchange temperatures indicated. There is an abrupt increase in threshold load at the shortest exchange time, and a gradual increase in P_{th} with increasing exchange time.

of the diffusion coefficient data using linearized coordinates from Equation 2, $\log_{10}(D)$ vs. $1/T$. The noise in the composition data is a source of considerable uncertainty in the estimation of the diffusion coefficient when the diffusion lengths are very small, and therefore only the three longest ion-exchange times, approximately 20, 30, and 60 min (Table II) were used to estimate diffusion coefficients. Error bars represent one standard deviation in the measured diffusion coefficient. The activation energy for diffusion was $Q = 0.75$ eV, and the prefactor $D_0 = 7.3 \times 10^{-9} \text{ m}^2 \text{ s}^{-1}$, both estimated from the linear fit shown in Fig. 5. A combination of Equations 1 and 2 may then be used to predict the degree of ion-exchange within the temperature range of these experiments (380–420°C).

3.2. Indentation cracking threshold

Fig. 6 is the result of the indentation threshold tests for all of the ion-exchange time-temperature combinations, including the unexchanged (as-received) glass. The most striking feature is the dramatic increase in P_{th} at very short exchange times. There are modest increases in P_{th} with further tempering. It should be noted that samples tempered for sixty minutes at all of the temperatures did not crack at loads within the capability of the indenter.

3.3. Indentation surface stress estimation

The stress-intensity factor, K^R , for a crack created by a sharp, geometrically similar indenter such as the Vickers pyramid, can be modeled by [24]

$$K^R = \frac{\chi P}{c^{3/2}}, \quad (3)$$

where P is the indentation load, c is the crack surface trace length (as measured from the center of the indentation impression), and χ is a semi-empirical stress-field

amplitude,

$$\chi = \xi \left(\frac{E}{H} \right)^{1/2}, \quad (4)$$

where E is the elastic modulus (70 GPa), H is the Vickers hardness (measured as 5.7 GPa for this glass), and ξ is a material-invariant constant, taken here as $\xi = 0.016 \pm 0.004$ [24]. At equilibrium, the stress-intensity factor of Equation 3 may be equated to the material toughness, T , which implies that

$$\frac{P}{c_0^{3/2}} = \frac{T}{\chi}. \quad (5)$$

The quantity $P/c^{3/2}$ is the indentation fracture parameter [24], where the subscript “0” indicates the crack length in the unstressed (base) glass.

The crack length at the threshold indentation load was measured and is plotted in Fig. 7. It is interesting to note that the relationship between crack length and threshold indentation load is linear, but the threshold load point for the base glass (square point) does not lie on the line. For comparison, the entire c - P relationship ($c \sim P^{2/3}$) for unexchanged glass is plotted.

Lawn and Fuller [18] derived the stress-intensity factor due to a strip of stress acting over a circular or semi-circular crack, with the intention of estimating surface stresses via indentation fracture. This configuration is shown in Fig. 8. For a general distribution of stress $\sigma(x)$ within a zone d situated at the surface of the semi-circular crack, the stress-intensity factor at the surface, K^s , is [18]

$$K^s = \frac{\psi^s}{c^{1/2}} \int_0^d [(c/x)^{1/2} - 1] \sigma(x) dx. \quad (6)$$

The Lawn and Fuller analysis is strictly for an embedded circular crack, but it is supposed that the factor ψ^s

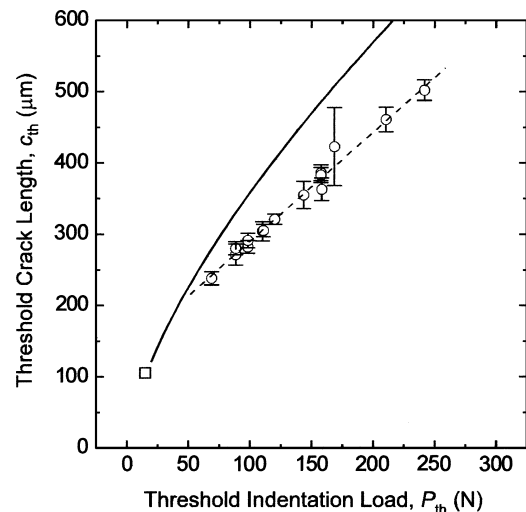


Figure 7 Radial crack length for the ion-exchanged ALS glass. The threshold indentation load for the unexchanged glass, 15 N, is shown as a square, and the crack length—indentation load relationship shown as a solid line. A dashed line indicates the linear relationship between threshold crack length and threshold indentation load for the exchanged glass.

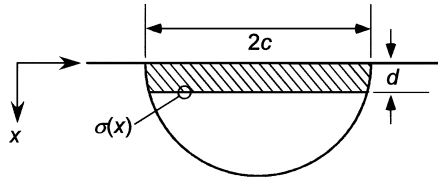


Figure 8 A schematic diagram of the fracture system used to estimate surface stresses via indentation fracture: an arbitrary stress distribution $\sigma(x)$ acts over the strip of depth d located at the mouth of a semi-circular surface crack. The computed stress-intensity factor of Equation 6 is at the surface.

sufficiently modifies the analysis to account for crack geometry and the free surface.

When the surface stress distribution is uniform over d and equal to σ^s , Equation 6 becomes [18]

$$K^s = \psi^s \sigma^s d^{1/2} [2 - (d/c)^{1/2}], \quad (7)$$

and when the strip extends the entire depth of the crack ($d = c$), Equation 7 reduces to the well-known result for a circular crack under uniform stress,

$$K^s = \psi^s \sigma^s c^{1/2}. \quad (8)$$

Alternatively, when the width of the strip of stress is very thin ($d \ll c$), Equation 6 reduces to

$$K^s = 2\psi^s \sigma^s d^{1/2}. \quad (9)$$

The local compressive stresses generated are proportional to the local amount of ion exchange [9, 23], in reaction to the imposed-volume-strain mechanism of stress generation in ion-exchange systems [2, 23]. Therefore, the surface stress distribution will ideally follow the surface distribution of excess K^+ (or depleted Na^+). However, ion-exchange for long times, or at temperatures near the softening point of the glass can result in relaxation of the surface stresses, marked by a deviation in the correspondence between composition and stress [25]. It has also been suggested that a change in thermal expansion coefficient of the ion-exchanged material can account for some, but not all, of the composition–stress deviation [26]. In this work, deviations from proportional composition–stress dependence will not be considered.

If the compressive stresses are indeed proportional to the K^+ concentrations, a complementary error function would most closely approximate the stress distribution, vis-à-vis

$$\sigma(x) = \sigma^s \left[1 - \operatorname{erf} \left(\frac{x}{2\sqrt{Dt}} \right) \right]. \quad (10)$$

The substitution of an error function into Equation 6 makes the form of K^s cumbersome. Often, the stress at the surface in an ion-exchanged glass is approximated by a linear stress profile [27],

$$\sigma(x) = \sigma^s (1 - x/d), \quad (x < d). \quad (11)$$

In this case, the resulting stress-intensity factor is [19]

$$K^s = \psi^s \sigma^s d^{1/2} [(4/3) - (d/4c)^{1/2}], \quad (12)$$

which reduces to

$$K^s = \frac{4}{3} \psi^s \sigma^s d^{1/2} \quad (13)$$

in the limit of $d \ll c$.

Extraction of an estimate of the surface stress from the $\sigma^s d^{1/2}$ product requires that the depth d of the compressive stresses be estimated. As a compromise between the known complementary error functional dependence of the K^+ ion (and presumably the compressive stresses) and the linearly-decreasing stress stress-intensity factor of Equation 13, d may be estimated as the length that matches the total “line-force” for the linearly-decreasing stress distribution of Equation 11 to the stress distribution proportional to local ion concentration, Equation 10.

$$\sigma_s \frac{2}{\pi^{1/2}} (Dt)^{1/2}. \quad (14)$$

Comparison with Equation 14 with the total line force from the triangular stress distribution of Equation 11,

$$\frac{\sigma_s d}{2}, \quad (15)$$

yields a *characteristic* ion-exchange depth, $\langle d \rangle$ of

$$\langle d \rangle = \frac{4}{\pi^{1/2}} (Dt)^{1/2}. \quad (16)$$

At $\langle d \rangle$ the complementary error function has decayed to 0.1% of the surface value, indicating that this is a good estimate for the ion-exchange depth.

We may combine Equations 3 and 13 to yield the total stress-intensity factor, K of a crack under combined surface stress and indentation elastic-plastic mismatch loading,

$$K = \frac{\chi P}{c^{3/2}} + \frac{4}{3} \psi^s \sigma^s d^{1/2}. \quad (17)$$

At equilibrium, $K = T$, and a combination of Equations 17 and 5 may be rearranged to form

$$\frac{P}{c^{3/2}} = \frac{P}{c_0^{3/2}} + \frac{4}{3} \frac{\psi^s}{\chi} \sigma^s d^{1/2}. \quad (18)$$

Equation 18 implies that the indentation fracture parameter, $P/c^{3/2}$, for a surface-stressed glass will be equal to that of the unstressed glass plus a constant, and will be invariant with indentation load (or crack length). Alternatively, a plot of the indentation fracture parameter as a function of $d^{1/2}$ will be linear and have a slope proportional to the $\psi^s \sigma^s$ product. Fig. 9 is a plot, in the manner of Equation 18, of $P/c^{3/2}$ for the ion-exchanged specimens of Table I as a function of the characteristic diffusion length $\langle d \rangle$. A solid line is shown as a best linear fit through the data, where the intercept has been fixed at the experimentally determined value

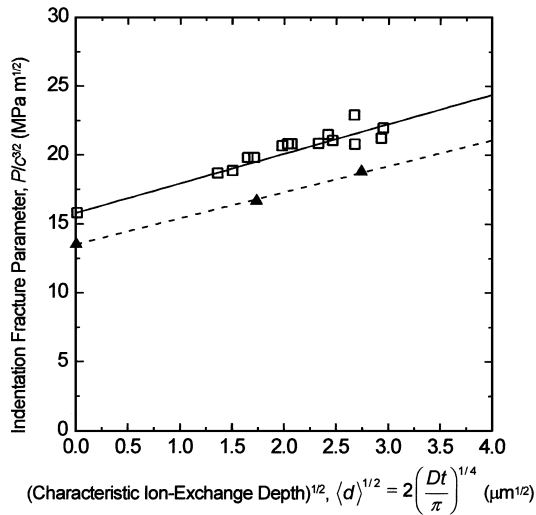


Figure 9 A plot of the indentation fracture parameter, $P/c^{3/2}$, as a function of $(d)^{1/2}$ for the ion-exchange time-temperature combinations in Table I (open squares). Fits to Equation 18 are shown. The geometry parameter ψ^s is found from the data of Green and Tandon [19] (solid triangles) to be approximately $\psi^s = 0.090$, leading to an estimation of the surface stress for the ion-exchange system here as $\sigma^s = -1000$ MPa.

of $P/c_0^{3/2} = 15.8 \text{ MPa}\sqrt{\text{m}}$ for the unexchanged glass over an indentation load range of 20–200 N.

Green and Tandon performed indentation stress-measurement experiments on ion-exchanged soda-lime glass [19] (the only other attempt of this method on an ion-exchanged silicate glass known to the authors). It was shown, for both ion-exchange conditions used, that the indentation fracture parameter was constant over a range of crack lengths, consistent with Equation 18. The average $P/c^{3/2}$ for each ion-exchanged glass (as well as $P/c_0^{3/2} = 13.5 \text{ MPa}\sqrt{\text{m}}$ for that particular glass) is plotted in Fig. 9 versus their own estimates of (d) , along with a best linear fit shown as a dashed line. It is evident, from our work and the work of others [19], that for ion-exchanged glasses, the *scaling* of Equation 18 is correct.

At this point it is necessary to discuss the value of ψ^s . It is usually assumed that ψ^s is approximately unity [18, 28], as it is only a free-surface modification to a complete theoretical solution for an embedded circular crack. Furthermore, it is normally expected that an experimental value of ψ^s derived from uniform-stress strength testing [29, 30] is sufficient because the uniform stress (Equation 8) and the thin-layer-of-stress (Equations 9 and 13) stress-intensity factors are limiting solutions of the general stress-intensity factor expression of Equation 6. There is no *prima facie* reason to believe that ψ^s varies due to details in the surface stress distribution.

However, there is some disagreement about the applicability of the indentation stress-measurement method. The method has been shown to predict correctly residual stresses of lightly (< 100 MPa) compressive thin films [28] on soda-lime glass using $\psi^s \approx 1$. The indentation method significantly underestimated independent stress estimates for heavily (> 1 GPa) compressive [31] dielectric thin films on soda-lime glass, ion-implanted ceramics and glasses [20, 21], and

possibly overestimated tensile stresses by up to a factor of two on proton-irradiated glass [18]. Green and Tandon calculated a surface stress for ion-exchanged glass (Fig. 9) that was a factor of ten too low, using $\psi^s = 0.73$ from fracture strength measurements [19]. It was observed that the radial/median cracks were “pinched” at the surface; that is, the crack front was arrested within the thin compressive surface layer and did not reach the surface. This same phenomenon has been observed by Burnett and Page [20] in ion-implanted materials, as well as by the authors for the current system. The crack geometry change caused by “pinching” at the surface has been deemed to be so severe as to radically change ψ^s , and therefore invalidate the premises upon which Equation 18 are built [19].

If the crack shape were extraordinarily different from the assumed half-penny shape, then the constant χ , coupling the indentation load to the stress-intensity factor at the crack tip (Equation 3), would ostensibly change as well. However, while the crack shape is affected near the compressive stress zone at the surface, it is still roughly semi-circular [19]. Also, it has been shown, experimentally [17] and theoretically [32], that Equation 3 remains valid for either the half-penny or radial crack geometries, and therefore it seems that χ will be insensitive to small changes in crack geometry.

An alternative interpretation of the discrepancy between the inferred and real surface stresses is that the arrest of the crack front within the surface compressive zone necessarily reduces the compressive stress acting over the crack surface (stresses not acting over crack surface do not contribute to the total stress intensity factor at the crack tip). The coupling term ψ^s between the surface stresses and the crack is therefore greatly diminished, but χ remains unchanged and ψ , coupling a uniform applied stress over such a crack, would remain of order unity. This, then, is a crack-shape effect; but it is one that only affects the stress-intensity contribution from very thin ($c \gg d$), very large *compressive* surface stresses. The scaling of the model (Equation 18) remains robust, evident from Fig. 9, and therefore a value of ψ^s can be calibrated from a comparison of independently measured stress values and the observed $\psi^s \sigma^s$ product. From the stress data of Green and Tandon [19] and the best fit line of Fig. 9, an average value of $\psi^s = 0.090 \pm 0.006$ is appropriate. This yields a representative stress value of $\sigma^s = -1000 \pm 75$ MPa for the ion-exchange system used here. Bradshaw [33] measured surface stresses of -550 to -700 MPa for this composition of glass; however, these stresses were measured after much longer ion-exchange times than used here (51–122 h). Dwivedi and Green measured a surface stress of -880 MPa for a 1 h exchange at 500°C [14]. In light of the shorter exchange times and lower temperatures used in this work, stress relaxation is probably negligible, and the surface stresses estimated by the indentation method seem reasonable.

4. Initiation fracture model

4.1. Background

Several models of crack initiation at indentation sites have been posited to explain the existence of the

indentation threshold for cracking [7, 12, 13]. Much previous work has noted the increase in resistance to indentation cracking when compressive stresses are introduced into the surface of glasses, by an increase in P_{th} on post-indentation observation [8] and a delay in radial crack initiation in the indentation load-unload cycle [10, 34]. Dal Maschio *et al.* [7] derived an expression for P_{th} in ion-exchanged soda-lime glass as part of a method of determining residual stress profiles. The analysis assumed that a pre-existing surface stress over the crack nucleus is essentially uniform. It should be noted that the residual stresses measured by this method extended up to $60 \mu\text{m}$ into the surface, and that the magnitude of the estimated stresses were no more than 150 MPa (compressive). The relatively small values of compressive stress in Dal Maschio's experiments were attributed to relaxation phenomena active at high temperatures and long exchange times in the soda-lime glass used.

Plastic deformation beneath the indenter generates a local zone of strain-mismatch, which gives rise to a localized hoop-tensile stress field that drives cracking at the indentation site [17, 24]. It is well established that indentation with a sharp indenter (such as a Vickers pyramid) generates cracks at the indentation site, irrespective of the pre-existing condition of the surface, which leads to the conclusion that sharp indentation must nucleate nascent flaws via the plastic deformation process [11, 35, 36]. It is also observed that radial cracks are usually formed at the corners of the impression [17]. Based on these observations, models of crack nucleation in soda-lime and aluminosilicate glasses at sharp contacts focus on the shear deformation mechanism that dominates plastic deformation under the high confining hydrostatic pressures of indentation [37, 38].

A model is developed in this paper that follows from the work of Cook and Braun [13], which utilizes a model to explain observations of indentation crack behavior in transformation-toughening yttria-tetragonal zirconia polycrystalline materials. Because compressive surface stresses can be viewed as a local toughening mechanism [34], many of the physical elements of this model may be used to explain the resistance to crack initiation that is caused by ion exchange. However, the inhomogeneity of the toughening due to surface stresses (as compared to a toughening mechanism that is uniformly distributed throughout the material, such as phase transformation) requires that the model be adapted to better suit the physical circumstances.

4.2. Residual indentation stress field

Fig. 10 schematizes the Vickers indentation impression, crack nucleus, and stress fields used to create the indentation threshold model. A crack nucleus is imagined to be created by the intersection of shear faults, which are roughly parallel to the faces of the Vickers indenter. The nascent radial crack flaw is contained within the deformation zone, and envisioned to be roughly semicircular. Within the deformation zone, stress is compressive, except near the edge of the zone where the stresses acting over a prospective radial crack increase to their max-

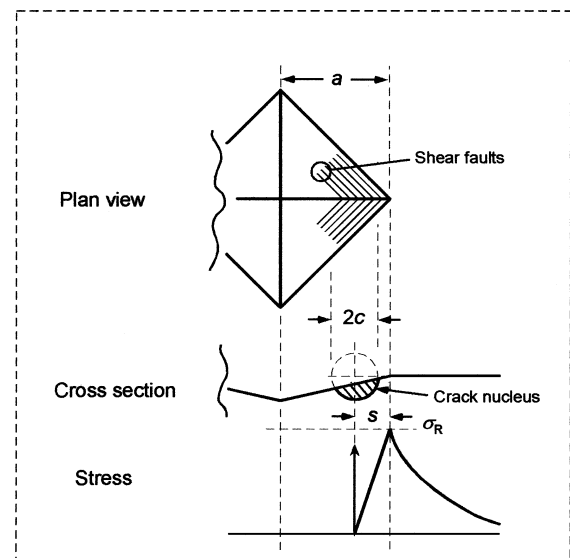


Figure 10 Schematic diagram of the geometry used in the crack initiation model. Shear faults intersect at indentation impression edges to create a radial crack nucleus of characteristic dimension c . A linearly increasing tensile stress acts over a length s , which unstably propagates the crack to a final stable configuration outside the indentation deformation zone.

imum at the edge of the zone. This stress increase is normally assumed to be linear,

$$\sigma_r^{\text{inner}}(r) = \sigma^R \left(\frac{r}{s} \right), \quad r < s, \quad (19)$$

where σ^R is the amplitude of the residual stresses and s is the extent of the tensile stress within the deformation zone. In this model, the center of the prospective radial crack is centered such that the tensile stress within the deformation zone acts over half of the crack. Outside the deformation zone, the tensile stresses decrease rapidly according to

$$\sigma_r^{\text{outer}}(r) = \sigma^R \left(\frac{a}{r + a - s} \right)^3, \quad r > s. \quad (20)$$

This is the familiar $1/r^3$ type stress field of an expanding cavity within an elastic medium, generally used to model the stress field at an elastic-plastic indentation [39–41]. The asymptote is chosen to be at the center of the indentation impression; a convention followed by many authors [12, 39–41], although others have chosen the asymptote to lie at the beginning of the tensile stress zone within the plastic deformation zone (the coordinate origin as defined in Fig. 10) [13].

The geometrical similarity of the problem allows for some simplification by non-dimensionalization. Dimensionless variables are set as [13]

$$\begin{aligned} \rho &= r/a \\ C &= c/a \\ S &= s/a \end{aligned} \quad (21)$$

where a is defined as the characteristic indentation impression dimension through the hardness, H , for a

Vickers indenter,

$$H = \frac{P}{2a^2}. \quad (22)$$

The normalized crack length, C , is constrained to be less than or equal to the dimensionless length of the intra-deformation zone tensile stress zone, S . With Fig. 10, a fracture-mechanics based description of the conditions necessary for crack initiation from shear-fault derived crack nuclei may be derived.

The stress-intensity factor for a circular crack under the action of a radially symmetric stress distribution is [42]

$$K(c) = \psi \frac{1}{C^{1/2}} \int_0^c \frac{r\sigma(r)dr}{(c^2 - r^2)^{1/2}}, \quad (23)$$

where ψ is an adjustable geometry parameter, such that $\psi = 2/\pi^{1/2}$ for an embedded circular crack under uniform applied stress [13]. We are concerned with the mechanics of radial crack initiation, and not stabilization, and therefore the stress field of Equation 19 is used to generate the stress-intensity factor that controls initiation of a shear-nucleated crack. Combination of Equation 19 with Equation 23, and normalizing via the variables of Equation 21, the stress-intensity factor takes the form

$$K(C) = \psi_{\text{nuc}}^{\text{inner}} a^{1/2} \frac{1}{c^{1/2}} \int_0^c \frac{\sigma_R \rho^2 d\rho}{S(C^2 - \rho^2)^{1/2}}, \quad (24)$$

where $\psi_{\text{nuc}}^{\text{inner}}$ is the geometry factor specifically coupling the tensile stress inside the deformation zone with the crack nucleus. The residual stress amplitude can be reduced to a dimensionless variable, α^R , via normalization by the material hardness,

$$\sigma^R = \alpha^R H. \quad (25)$$

Completion of the integral in Equation 24 gives the stress-intensity factor as

$$K(C) = (Ha^{1/2}) \frac{\pi}{4} \psi_{\text{nuc}}^{\text{inner}} \alpha^R \frac{C^{3/2}}{S} = P_{\text{th}}^{1/4} \left(\frac{T}{P_{\text{th},0}^{1/4}} \right), \quad (26)$$

which is the product of a load-dependent scaling term, $(Ha^{1/2})$, and a scale-invariant geometrical term. The increasing stress within the deformation zone gives rise to a strongly destabilizing stress-intensity factor field—stronger than a uniform tensile stress stress-intensity factor ($K \sim c^{1/2}$). By setting Equation 26 equal to the material toughness, T , and substituting in the hardness relationship (Equation 25), the indentation threshold load in the unstressed material, $P_{\text{th},0}$ can be found in terms of the critical dimensionless crack nucleus size, C_{nuc} :

$$P_{\text{th},0}^{1/4} = \frac{T}{H^{3/4}} \frac{2^{9/4}}{\pi \psi_{\text{nuc}}^{\text{inner}} \alpha^R} \frac{S}{C_{\text{nuc}}^{3/2}}. \quad (27)$$

When P is equal to or larger than P_{th} , the nascent crack flaw will propagate unstably out of the deformation zone until stable equilibrium ($K = T$, $dK/dc < 0$) is reached in the diminishing, farfield stress of Equation 20.

4.3. Ion-exchange stress field

Description of the effect of the ion-exchange stresses on crack initiation is difficult, because the compressive stresses generated by the ion-exchange process decrease sharply with depth into the material. Furthermore, the ion-exchange stress field breaks the geometrical similarity between the indentation impression size, crack nucleus, and net stress field. In this model, we use the stress-intensity factor of Equation 12 [19] to describe the effects of the ion-exchange stresses on the crack nucleus.

Because the ion-exchange depth does not share similarity with the indentation contact, only the crack size may be normalized, which transforms Equation 12 into

$$K_{\text{nuc}}^s = \psi_{\text{nuc}}^s \sigma^s d^{1/2} \left[\left(\frac{4}{3} \right) - \frac{1}{2a^{1/2}} (d/C_{\text{nuc}})^{1/2} \right]. \quad (28)$$

Combination of Equations 26 and 28 yields the total stress-intensity factor for the crack nucleus under the influence of the residual and ion-exchange stress fields:

$$K_{\text{nuc}}^{\text{total}} = (Ha^{1/2}) \frac{\pi}{4} \psi_{\text{nuc}}^{\text{inner}} \alpha^R \frac{C_{\text{nuc}}^{3/2}}{S} + \psi_{\text{nuc}}^s \sigma^s d^{1/2} \times \left[\left(\frac{4}{3} \right) - \frac{1}{2a^{1/2}} (d/C_{\text{nuc}})^{1/2} \right]. \quad (29)$$

Using the relationship between the indentation load P and the impression dimension a (Equation 22), and equating the stress-intensity factor to the toughness at incipient radial crack formation, Equation 29 becomes

$$K_{\text{nuc}}^{\text{total}} = T = P_{\text{th}}^{1/4} \frac{T}{P_{\text{th},0}^{1/4}} + \frac{4}{3} \psi_{\text{nuc}}^s \sigma^s d^{1/2} - \frac{1}{P_{\text{th}}^{1/4}} \psi_{\text{nuc}}^s \sigma^s d^{1/2} \left(\frac{3H^{1/4}}{2^{3/4}} \frac{d^{1/2}}{C_{\text{nuc}}^{1/2}} \right), \quad (30)$$

If it is recognized that within Equation 30 there is a stress-intensity factor-like term due to the surface stresses that is independent of any indentation or crack-length variable, we may define it as a toughening [43, 44], here, called the *surface-stress initiation toughening*, T^s :

$$T^s = -\frac{4}{3} \psi_{\text{nuc}}^s \sigma^s d^{1/2} \quad (31)$$

where the negative sign is included so that compressive surface stresses naturally increase the initiation threshold. Equation 30 may be rearranged to yield a solution for P_{th} in terms of the initiation threshold in the

unstressed glass,

$$P_{th}^{1/4} = \frac{P_{th,0}^{1/4}}{2T} \left\{ (T + T^s) + \left[(T + T^s)^2 - \frac{3H^{1/4}}{2^{3/4}} \frac{TT^s}{P_{th,0}^{1/4}} \left(\frac{\langle d \rangle}{C_{nuc}} \right)^{1/2} \right]^{1/2} \right\}. \quad (32)$$

Similar expressions for T^s and the initiation threshold load may easily be derived for a strip of uniform stress at the surface (Equation 7). The use of T^s makes Equation 32 reducible to a form similar to that expected for a change in homogeneously-distributed material toughness, ΔT (with no other change in material properties),

$$P_{th}^{1/4} = \frac{P_{th,0}^{1/4}}{T} (T + \Delta T), \quad (33)$$

except that the increase in the initiation threshold for the surface-stressed material involves a cross-term that contains information about the length scales of the surface stress and the crack nucleus. If the stress is uniform over the crack nucleus, the expression for P_{th} is

$$\begin{aligned} P_{th}^{1/4} &= \frac{TP_{th,0}^{1/4}(2H)^{1/4}}{T(2H)^{1/4} + \psi_{nuc}^s \sigma^s C_{nuc}^{1/2} P_{th,0}^{1/4}} \\ &= P_{th,0}^{1/4} \frac{T}{(T - T^s)}, \end{aligned} \quad (34)$$

identical in form to the expression derived by Dal Maschio *et al.* [7]. It can readily be verified that the surface-stress initiation toughening for uniform stress is $T^s = -\psi_{nuc}^s \sigma^s C_{nuc}^{1/2} a_{th,0}^{1/2}$, where $a_{th,0}$ is the hardness impression dimension at the threshold load in the unstressed material.

4.4. Application of the model to experimental data

The results of Fig. 9 indicate that there is a single representative value of the characteristic surface stress, σ^s . If σ^s is chosen to be fixed for every experiment, then Equation 30 is a varying function of d only. For consistency with the crack length line force estimation results, the depth of the stress, d , acting over a nascent radial crack will be estimated as the characteristic ion-exchange depth, $\langle d \rangle$, as per Equation 16.

Inspection of Equation 32 suggests that $P_{th}^{1/4}$ is roughly linear in $\langle d \rangle^{1/2}$, and therefore these are used as the dependent and independent variables for data fitting in Fig. 11. The fixed parameters in the model are set as follows: $P_{th,0} = 15$ N, $\sigma^s = -1000$ MPa, $H = 5.7$ GPa, and $T = 0.9$ MPa \sqrt{m} from indentation toughness estimation (Equation 5). The best fit of Equation 32 shown in Fig. 11 as a solid line, with the best fit parameters $\psi_{nuc}^s = 0.267 \pm 0.02$ and $C_{nuc} = 0.170 \pm 0.09$. If the surface-stress initiation toughening (Equation 31) is approximated as a homogeneous toughness increase (Equation 33), then the predicted increase in initiation

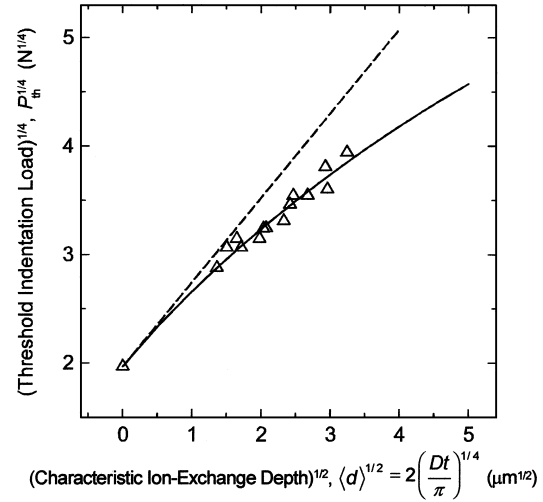


Figure 11 Indentation cracking threshold data of Fig. 6 replotted in the manner of Equation 32, $P_{th}^{1/4}$ vs. $\langle d \rangle^{1/2}$. The solid line is a best fit of the full indentation threshold model, Equation 32, and the dashed line is the asymptotic approximation of Equation 33, with the change in toughness approximated as T^s .

threshold (with $\psi_{nuc}^s = 0.267$ and $\sigma^s = -1000$ MPa) is shown in Fig. 11 as a dashed line.

5. Discussion

A fracture-mechanics based model for the indentation threshold load in Na^+ - K^+ ion-exchanged ALS glass has been derived and shown to describe experimental data over a wide range of exchange conditions. The threshold load is a measure of the conditions for initiation of a metastable crack nucleus, located within the indentation contact deformation zone, into a well-developed radial crack, extending beyond the zone boundary. The physical basis of the model is that on increasing indentation load there is a competition between the increasing size of the nucleus and the indentation tensile zone (which favor initiation) and the concomitant extent into the compressive ion-exchange field (which opposes initiation). The threshold load is then a measure of the critical contact dimension at which the crack driving force deriving from the combination of nucleus and zone sizes surpasses the resistive forces associated with material toughness and compressive stress effects.

The expected threshold load change has been shown to be dependent on two terms: a characteristic surface toughening parameter, independent of any crack nucleus size, and another term that relates the relative scale of the surface stresses and the crack nucleus. The characteristic surface toughening is analogous to a homogeneous toughening mechanism (for example, the inclusion of a pressure-induced phase-transforming material in a matrix). The model partially bridges two limiting effects on the initiation behavior—that of uniform *toughening*, and that of uniform superimposed *stress*. Fig. 12 is a plot that reproduces the fit of Fig. 11 over a broader range. Also shown in Fig. 12 is the expected increase in threshold with the surface-stress toughening-only approximation (with constant $\psi_{nuc}^s = 0.267$ and $\sigma^s = -1000$ MPa) and the threshold

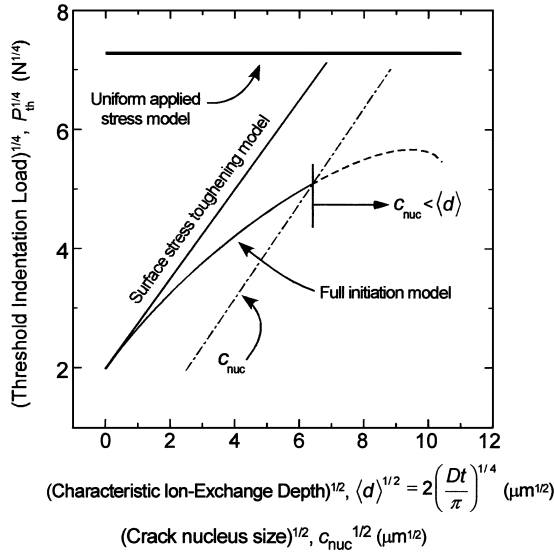


Figure 12 Indentation cracking threshold load vs. characteristic ion-exchange depth. The fit to the full indentation model from Figure 11 is shown, as well as the surface-stress indentation toughening approximation (Equation 33) and uniform stress model (Equation 34). All $P_{th}^{1/4}$ vs. $\langle d \rangle^{1/2}$ relations were generated with $\psi_{nuc}^s = 0.267$ and $\sigma^s = -1000$ MPa. The crack nucleus dimension, c_{nuc} , is plotted as well. When $\langle d \rangle$ exceeds c_{nuc} , the full indentation model is invalid. At very small $\langle d \rangle$, the surface-stress indentation toughening approximation is accurate; at very large $\langle d \rangle$, the uniform stress model is appropriate.

with a uniform applied stress ($\sigma^s = -1000$ MPa). The triangular strip-of-stress stress-intensity-factor solution (Equation 12) requires that $c > d$ to be applicable [18], which means that the full threshold model breaks down when $c_{nuc} < \langle d \rangle$. A line of calculated c_{nuc} is shown in Fig. 12—when c_{nuc} exceeds $\langle d \rangle$, neither the model of Equation 32 nor the uniform superimposed stress model of Equation 34 strictly applies. A bridging model can be derived for $c_{nuc} > \langle d \rangle > \infty$ that is cubic in $P_{th}^{1/4}$ using the results of Lawn and Fuller [18]; however, the result is complicated and not needed in this work. For the large stresses and shallow residual stress depths in the tempered glass system here, this is unlikely to be a practical complication—the model shown is expected to hold until a threshold load of 1600 N is reached. However, it may become more important for systems with deeper residual stress depths, or for indenter geometries that can reduce the cracking threshold to scales commensurate with the scale of the residual stress depth, such as a cube-corner pyramid [45].

The geometry factor coupling the surface stress to the crack nucleus, $\psi_{nuc}^s = 0.267$, is considerably less than the normally expected $\psi^s \approx 1$ (Section 3.3). This may be due to several factors, such as the shape and orientation of the nucleus. The geometry factor coupling the residual indentation stress field to the crack nucleus is estimated from the micromechanical description of the threshold load in the unstressed glass (Equation 27) as $\psi_{nuc}^{inner} = 0.41$, with $C_{nuc} = 0.17$, and $\alpha^R = 0.170$ and $S = 0.148$ from the elastic-plastic analysis of Chiang *et al.* [39]. Although the observed $C_{nuc} > S$, which implies, within the framework of the model, that the crack nucleus is not contained within the hardness impression (see Fig. 10), the discrepancy is not important considering the uncertainty involved in estimation of C_{nuc} and S .

C_{nuc} and ψ_{nuc}^{inner} are not independently estimable from the threshold load in the unstressed material, and the agreement between ψ_{nuc}^{inner} and ψ_{nuc}^s demonstrates that while the crack nuclei are somewhat unlike a semi-circular surface-located crack ($\psi^s \approx 1$), the assumed geometry of the problem and subsequent threshold load scaling models are consistent.

It is noted that an implicit assumption in Equation 32 is that the magnitude of C_{nuc} is unaffected by the ion-exchange process. This seems reasonable in light of the experimental observation that plastic deformation, as measured by the hardness, H , is largely unaffected by the tempering treatment. C_{nuc} could certainly be quite different from material to material, if the dominant mode of plastic deformation were to change (for example, the predominant densification mode of deformation for fused silica vs. the shear-slip mode of deformation as for the glass used here). The dominant effect of an isolated change in C_{nuc} due to plasticity mechanism modifications or changes (as might be the case, for example, for ion-implanted glasses and ceramics [20, 21]) would be pronounced in the unstressed-material threshold load through a $P_{th,0} \sim C_{nuc}^{-6}$ dependence (Equation 27). For example, a 10% reduction in C_{nuc} will double the threshold load.

As part of the experimental programme, kinetic data for ion-exchange in this system have also been measured. A combination of the kinetic data and fracture mechanics allows us to construct a map of the indentation threshold for a range of ion-exchange time-temperature conditions. Fig. 13 is a contour plot of the predicted indentation cracking threshold load as a function of ion-exchange temperature and time. The temperature range of the predictions has been extended $\pm 30^\circ\text{C}$ from the experimental conditions, and the exchange time has been extrapolated to 120 min. Fig. 13 demonstrates compactly the experimental observation that there is an abrupt increase in P_{th} for very short exchange times, regardless of the exchange temperature. Unsurprisingly, exchange at higher temperatures leads to a greater penetration of K^+ into the surface of the

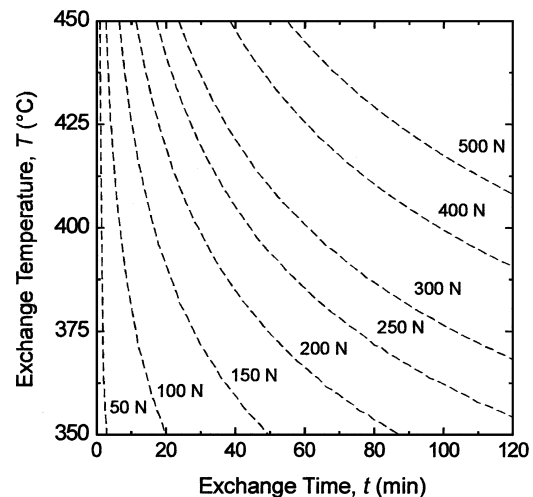


Figure 13 Map of predicted indentation crack threshold load, P_{th} , as a function of ion-exchange time and temperature, generated with the kinetic data of Equation 2 and the fracture model of Equation 32 with parameters found from the fit of Fig. 11.

glass, and a correspondingly larger P_{th} , with respect to time.

Fig. 13 is only a guide to the expected amount of contact fracture resistance conferred on an ion-exchanged glass; many deviations can be expected in practice. There is considerable uncertainty in determination of the threshold load, evident from Fig. 3. Also, only the degree of radial crack initiation attenuation is considered: at larger loads than those used here, critical subsurface flaws may initiate beneath the indenter (the median crack system) [17]. It may well be that surface stresses have a diminishing effect on the subsurface initiating mechanics, and therefore strength-degrading flaws may be initiated outside the framework of the current analysis. However, it may be concluded that the compressive stresses of ion-exchange not only strengthen a component with a pre-existing flaw population, but buttress that improved strength with increased damage resistance.

Also, this work is concerned only with the radial cracking system and not lateral cracking (i.e., cracks approximately parallel to the surface). This is the cracking system responsible for chipping and wear of surfaces. It was observed here, as well as elsewhere [10], that lateral cracking is somewhat enhanced by surface compressive stresses. While lateral cracking is an important damage mechanism, it is not particularly deleterious to brittle strength. Therefore, Fig. 13 is not a useful tool if surface wear or retention of optical quality under abrasive conditions is a concern.

Acknowledgement

The authors would like to thank S. Jill Glass (Sandia National Laboratories, Albuquerque, NM) for providing the ALS glass.

References

1. I. W. DONALD, *J. Mater. Sci.* **24** (1989) 4177.
2. R. F. BARTHOLOMEW and H. M. GARFINKEL, in "Glass: Science and Technology," Vol. 5, edited by D. R. Uhlmann and N. J. Kreidl (Academic Press, New York, 1980) p. 217.
3. R. TANDON and D. J. GREEN, *J. Amer. Ceram. Soc.* **74** (1991) 1981.
4. D. J. GREEN, *ibid.* **66** (1983) 807.
5. S. MALKIN and J. E. RITTER, *Key. Eng. Mat.* **71** (1992) 195.
6. J. E. RITTER, K. JAKUS and R. P. PANAT, in Materials Research Society Symposium Proceedings, Vol. 531, San Francisco, CA, edited by E. Suhir, M. Fukuda and C. R. Kurkjian (Materials Research Society, Warrendale, PA, 1998) p. 53.
7. R. DAL MASCHIO, V. M. SGLAVO and G. D. SORARU, *Mat. Sci. Eng.-A Struct. A* **119** (1989) L9.
8. V. R. HOWES, *J. Mater. Sci. Lett.* **1** (1982) 341.
9. R. TANDON, D. J. GREEN and R. F. COOK, *J. Amer. Ceram. Soc.* **73** (1990) 2619.
10. R. TANDON and R. F. COOK, *ibid.* **76** (1993) 885.
11. B. R. LAWN and A. G. EVANS, *J. Mater. Sci.* **12** (1977) 2195.

12. S. LATHABAI, J. RODEL, T. DABBS and B. R. LAWN, *ibid.* **26** (1991) 2157.
13. R. F. COOK and L. M. BRAUN, *ibid.* **29** (1994) 2192.
14. P. J. DWIVEDI and D. J. GREEN, *Fractogr. Glass. Ceram.* **III** (1996) 473.
15. D. C. JOY, "Monte Carlo Modeling for Electron Microscopy and Microanalysis" (Oxford University Press, New York, 1995).
16. D. C. JOY, Monte Carlo Simulations of Electron Beam—Solid Interactions, Computer Programme—PHIROZ. Available at <http://www.microscopy.com> or mirrored at <http://www.amc.anl.gov/ANLSoftwareLibrary>. Copyright 1991.
17. R. F. COOK and G. M. PHARR, *J. Amer. Ceram. Soc.* **73** (1990) 787.
18. B. R. LAWN and E. R. FULLER, *J. Mater. Sci.* **19** (1984) 4061.
19. D. J. GREEN and R. TANDON, in "Advances in Fracture Research," Vol. 4, Houston, TX, edited by K. Salama, K. Ravi-Chandar, D. M. R. Taplin and P. Rama Rao (Pergamon Press, Elmsford, NY, 1989) p. 2757.
20. P. J. BURNETT and T. F. PAGE, *J. Mater. Sci.* **20** (1985) 4624.
21. S. J. BULL and T. F. PAGE, *ibid.* **23** (1988) 4217.
22. S. URNES, *J. Amer. Ceram. Soc.* **56** (1973) 514.
23. A. J. BURGGRAAF and J. CORNELISSEN, *Phys. Chem. Glasses* **5** (1964) 123.
24. G. R. ANSTIS, P. CHANTIKUL, B. R. LAWN and D. B. MARSHALL, *J. Amer. Ceram. Soc.* **64** (1981) 533.
25. A. J. BURGGRAAF, *Phys. Chem. Glasses* **7** (1966) 169.
26. V. TYAGI and A. K. VARSHNEYA, *J. Non-Cryst. Solids* **238** (1998) 186.
27. B. R. LAWN and D. B. MARSHALL, *Phys. Chem. Glasses* **18** (1977) 7.
28. M. F. GRUNINGER, B. R. LAWN, E. N. FARABAUGH and J. B. JR. WACHTMAN, *J. Amer. Ceram. Soc.* **70** (1987) 344.
29. R. TANDON and D. J. GREEN, *ibid.* **73** (1990) 970.
30. D. B. MARSHALL and B. R. LAWN, *ibid.* **63** (1980) 532.
31. P. H. KOBRIN and A. B. HARKER, *J. Mater. Sci.* **24** (1989) 1363.
32. M. T. LAUGIER, *J. Amer. Ceram. Soc.* **68** (1985) C51.
33. W. BRADSHAW, *J. Mater. Sci.* **14** 2981.
34. R. TANDON, D. J. GREEN and R. F. COOK, *Acta Metall. Mater.* **41** (1993) 399.
35. B. R. LAWN, T. P. DABBS and C. J. FAIRBANKS, *J. Mater. Sci.* **18** (1983) 2785.
36. J. T. HAGAN and M. V. SWAIN, *J. Phys. D-Appl. Phys.* **11** (1978) 2091.
37. J. T. HAGAN, *J. Mater. Sci.* **14** (1979) 2975.
38. J. T. HAGAN and S. VAN DER ZWAAG, *J. Non-Cryst. Solids* **64** (1984) 249.
39. S. S. CHIANG, D. B. MARSHALL and A. G. EVANS, *J. Appl. Phys.* **53** (1982) 298.
40. E. H. YOFFE, *Phil. Mag. A* **46** (1982) 617.
41. K. TANAKA, *J. Mater. Sci.* **22** (1987) 1501.
42. H. TADA, P. C. PARIS and G. R. IRWIN, "The Stress Analysis of Cracks Handbook" (ASME Press, New York, 2000).
43. R. TANDON, D. J. GREEN and R. F. COOK, *Acta Metall. Mater.* **41** (1993) 399.
44. D. J. GREEN, R. TANDON and V. M. SGLAVO, *Science* **283** (1999) 1295.
45. D. S. HARDING, W. C. OLIVER and G. M. PHARR, in Materials Research Society Symposium Proceedings, Vol. 356S, edited by P. Baker, P. Borgesen, P. H. Townsend, C. A. Ross and C. A. Volkert (Warrendale, PA, 1995) p. 663.

Received 4 April

and accepted 5 December 2003